

Supporting Information
for
Theoretical and Experimental Characterization of Adsorbed CO and NO
on γ -Al₂O₃-supported Rh Nanoparticles

Alexander J. Hoffman¹, Chithra Asokan², Nicholas Gadinis², Pavlo Kravchenko¹, Andrew
(Bean) Getsoian³, Phillip Christopher^{2*}, David Hibbitts^{1*}

¹Department of Chemical Engineering, University of Florida, Gainesville, FL 32611, USA

²Department of Chemical Engineering, University of California Santa Barbara, Santa Barbara, CA 93106, USA

³Research and Advanced Engineering, Ford Motor Company, Dearborn, MI 48121, USA

*Corresponding authors: pchristopher@ucsb.edu, hibbitts@che.ufl.edu

Table of Contents

Section S1. Additional computational details.....	S4
Section S2. CO* binding to Rh(111).....	S5
Section S3. Diameter estimation from HRSTEM of 10 wt% Rh/ γ -Al ₂ O ₃ sample	S10
Section S4. CO* binding to Rh ₂₀₁ nanoparticles	S11
Section S5. NO* binding to Rh(111).....	S15
Section S6. NO* binding to Rh ₂₀₁ nanoparticles	S17
Section S7. NO-CO mixtures and exchange.....	S20
References.....	S21

List of Figures and Tables

Figure S1	S5
Figure S2.....	S6
Figure S3.....	S7
Table S1	S8
Table S2	S8
Table S3	S9
Figure S4	S9
Figure S5	S11
Figure S6	S12
Figure S7	S12
Figure S8	S13
Figure S9	S13
Figure S10	S14
Figure S11	S15
Table S4	S16
Figure S12	S16
Figure S13	S17

Figure S14	S18
Figure S15	S19
Figure S16	S19
Figure S17	S20
Figure S18	S20

Section S1. Additional computational details

Enthalpies (H) and Gibb's free energies (G) can be calculated from density functional theory (DFT)-derived energies using statistical mechanics. Specifically, each is a sum of the electronic energy (E_0), the zero-point vibrational energy (ZPVE), and the respective vibrational, translational, and rotational components of the species:

$$H = E_0 + ZPVE + H_{vib} + H_{rot} + H_{trans} \quad (\text{S1})$$

$$G = E_0 + ZPVE + G_{vib} + G_{rot} + G_{trans} \quad (\text{S2})$$

at 473 K. Adsorbed species are not considered to have translational or rotational contributions; all such motions are modeled as frustrated vibrations on the surface. Metal atoms of the Rh(111) surfaces and on the Rh₂₀₁ nanoparticles are frozen in place during frequency calculations. Vibrational, rotational, and translational enthalpies and free energies are estimated from other statistical mechanics formalisms:

$$ZPVE = \sum_i \left(\frac{1}{2} h\nu_i \right) \quad (\text{S3})$$

$$H_{vib} = \sum_i \left(\frac{h\nu_i \exp\left(-\frac{h\nu_i}{kT}\right)}{1 - \exp\left(-\frac{h\nu_i}{kT}\right)} \right) \quad (\text{S4})$$

$$G_{vib} = \sum_i \left(-kT \ln \left(\frac{1}{1 - \exp\left(-\frac{h\nu_i}{kT}\right)} \right) \right) \quad (\text{S5})$$

$$H_{trans} = \frac{5}{2} kT \quad (\text{S6})$$

$$H_{rot,linear} = kT \quad (\text{S7})$$

$$H_{rot,nonlinear} = \frac{3}{2} kT \quad (\text{S8})$$

$$G_{trans} = -kT \ln \left(\left(\frac{2\pi mkT}{h^2} \right)^{\frac{3}{2}} V \right) \quad (\text{S9})$$

$$G_{rot} = -kT \ln \left(\frac{1}{\sigma} \left(\frac{T^3}{\theta_x \theta_y \theta_z} \right)^{\frac{1}{2}} \right) \quad (\text{S10})$$

$$\theta_i = \frac{h^2}{8\pi^2 I_i k} \quad (\text{S11})$$

where I_i is the moment of inertia about the i axis (either x, y, or z) and σ is the symmetry number of the species.¹

Section S2. CO* binding to Rh(111)

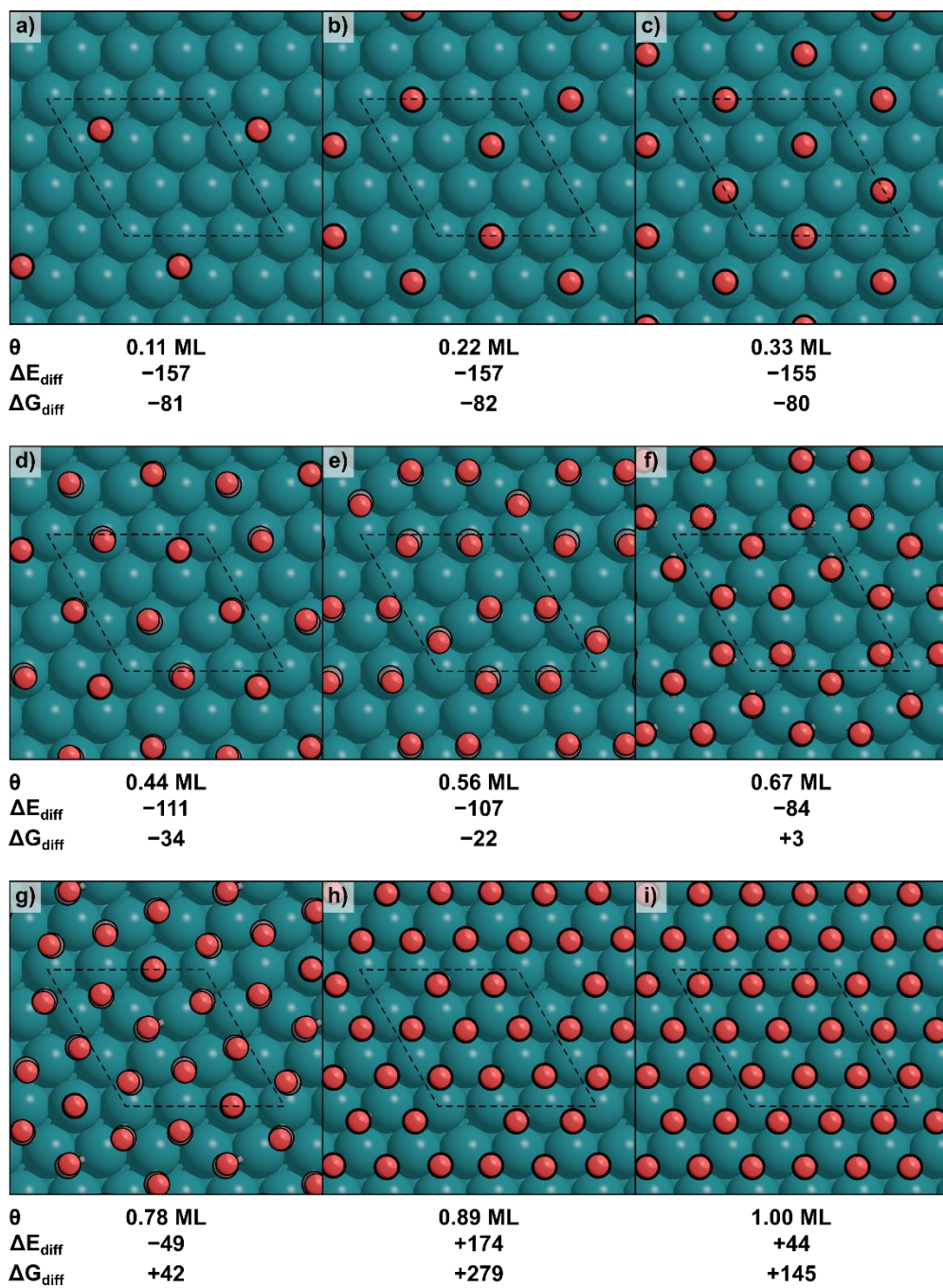


Figure S1. The lowest energy CO* binding modes from 0.11–1.00 ML on Rh(111). Differential binding electronic energies (ΔE_{diff}) and free energies (ΔG_{diff}) are shown beneath each corresponding structure in kJ mol⁻¹.

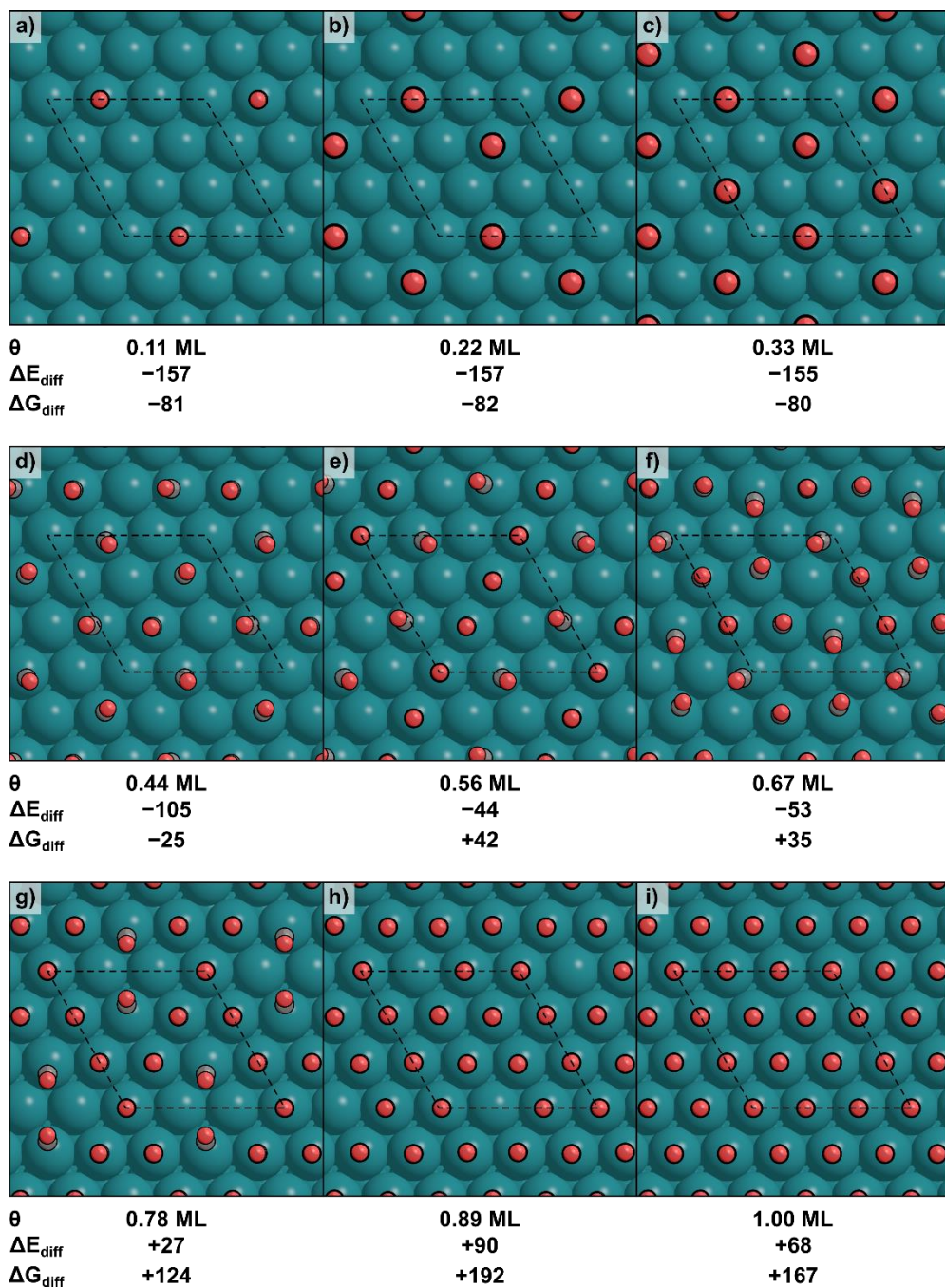


Figure S2. The lowest energy CO* binding modes with all CO* bound atop from 0.11–1.00 ML on Rh(111). Differential binding electronic energies (ΔE_{diff}) and free energies (ΔG_{diff}) are shown beneath each corresponding structure in kJ mol^{-1} .

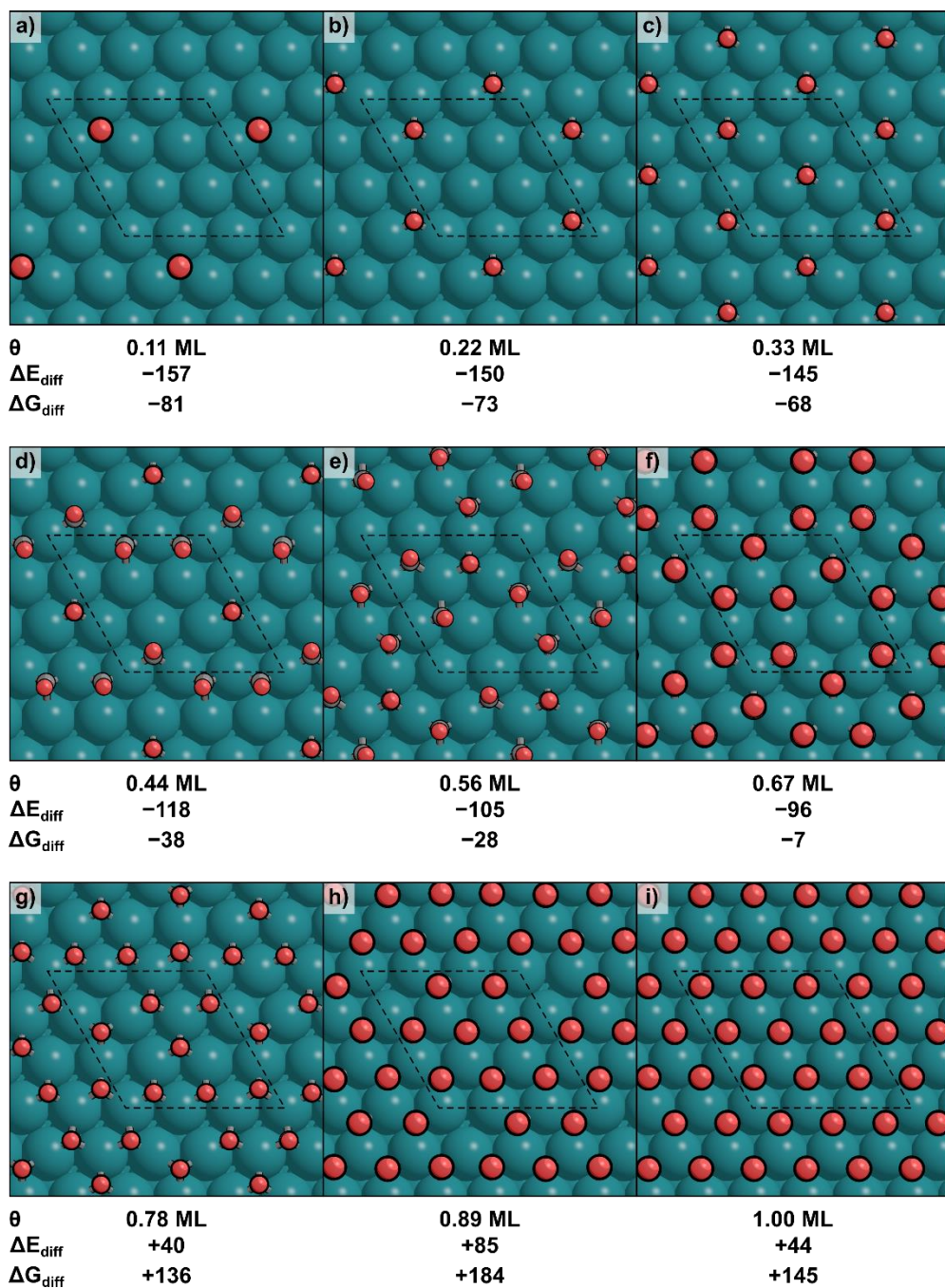


Figure S3. The lowest energy CO* binding modes with all CO* bound 3-fold from 0.11–1.00 ML on Rh(111). Differential binding electronic energies (ΔE_{diff}) and free energies (ΔG_{diff}) are shown beneath each corresponding structure in kJ mol^{-1} .

The two frequencies with the highest calculated intensities for different configurations of CO* on Rh(111) analyzed in this work are shown below in Tables S1–S3. In each case, the highest frequency was also the most intense, with the exception of the most stable adlayer configuration at 0.78 ML (Table S1), where the asymmetric stretch at 1937 cm⁻¹ had a larger intensity (15.3) than the maximum frequency at 2075 cm⁻¹ (8.7, also the second most intense frequency).

Table S1. DFT-calculated frequencies (ν_{CO} , all scaled by $\times 1.019$) and their predicted intensities for the most intense and second most intense frequencies of CO* on Rh(111) for the lowest energy configuration (including atop, 3-fold, and mixed binding modes) from 0.11–1.00 ML.

$\theta_{\text{CO}} / \text{ML}$	Binding mode	Most intense frequency		Second most intense frequency	
		$\nu_{\text{CO}} / \text{cm}^{-1}$	Intensity	$\nu_{\text{CO}} / \text{cm}^{-1}$	Intensity
0.11	3-fold hcp	1749	11.9		
0.22	atop	2018	35.3	1991	0.1
0.33	atop	2031	43.9	1993	0.0
0.44	mixed	2035	24.4	1783	8.3
0.56	mixed	2048	20.8	1839	10.6
0.67	3-fold mixed	1926	24.8	1847	0.0
0.78	mixed	1937	15.3	2075	8.7
0.89	3-fold fcc	1960	19.5	1854	0.1
1.00	3-fold fcc	1976	19.0	1883	0.0

Table S2. DFT-calculated frequencies (ν_{CO} , all scaled by $\times 1.019$) and their predicted intensities for the most intense and second most intense frequencies of CO* on Rh(111) for the lowest energy configuration where all CO* are bound atop from 0.11–1.00 ML.

$\theta_{\text{CO}} / \text{ML}$	Binding mode	Most intense frequency		Second most intense frequency	
		$\nu_{\text{CO}} / \text{cm}^{-1}$	Intensity	$\nu_{\text{CO}} / \text{cm}^{-1}$	Intensity
0.11	atop	2003	21.3		
0.22	atop	2018	35.3	1991	0.1
0.33	atop	2031	43.9	1993	0.0
0.44	atop	2043	42.2	1987	0.5
0.56	atop	2068	36.4	1988	3.4
0.67	atop	2074	36.4	2000	0.6
0.78	atop	2097	34.0	1991	0.4
0.89	atop	2116	31.4	2001	0.0
1.00	atop	2163	18.9	2093	10.4

Table S3. DFT-calculated frequencies (ν_{CO} , all scaled by $\times 1.019$) and their predicted intensities for the most intense and second most intense frequencies of CO^* on Rh(111) for the lowest energy configuration where all CO^* are bound 3-fold from 0.11–1.00 ML.

$\theta_{\text{CO}} / \text{ML}$	Binding mode	Most intense frequency		Second most intense frequency	
		$\nu_{\text{CO}} / \text{cm}^{-1}$	Intensity	$\nu_{\text{CO}} / \text{cm}^{-1}$	Intensity
0.11	3-fold hcp	1749	11.9		
0.22	3-fold hcp	1771	19.3	1751	0.0
0.33	3-fold hcp	1788	24.2	1756	0.0
0.44	3-fold mixed	1891	21.5	1793	3.2
0.56	3-fold mixed	1899	24.8	1819	0.8
0.67	3-fold mixed	1926	24.8	1847	0.0
0.78	3-fold mixed	1940	21.7	1842	0.3
0.89	3-fold fcc	1960	19.5	1854	0.1
1.00	3-fold fcc	1976	19.0	1883	0.0

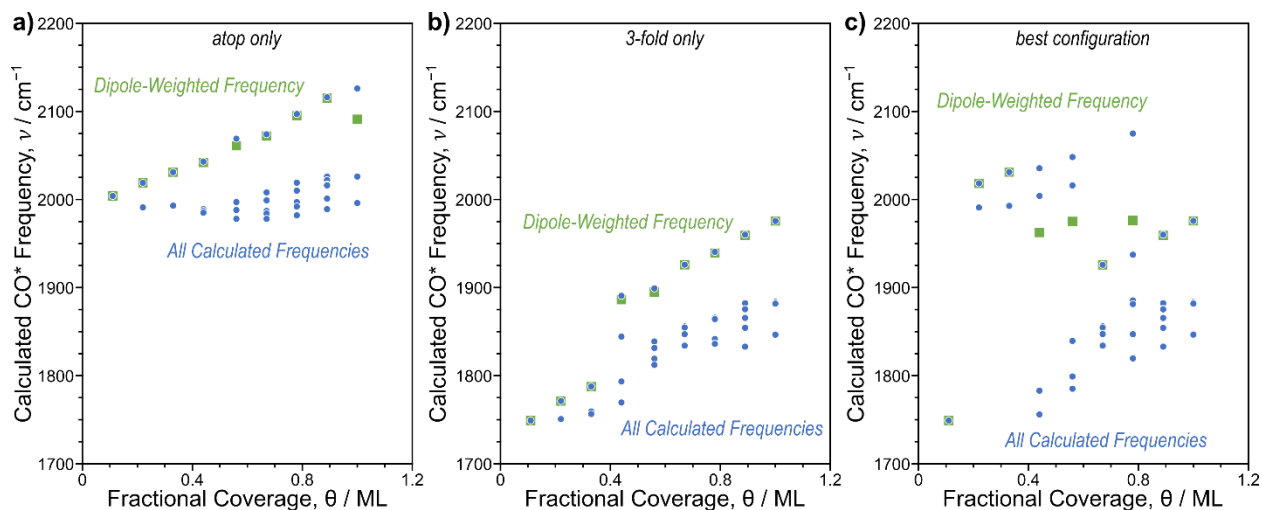


Figure S4. All calculated frequencies for CO^* on Rh(111) from 0.11–1.00 ML (\bullet , blue) with (a) all CO^* bound atop, (b) all CO^* bound 3-fold, and (c) in the most favorable configuration. The average frequency based on weights derived from DFT-predicted intensities with the estimated dipole are shown at each coverage (\blacksquare , green).

Section S3. Diameter estimation from HRSTEM of 10 wt% Rh/ γ -Al₂O₃ sample

The diameter d_i of each particle used for the particle size distribution was calculated from the particle area using a circular cross-section area formula; these diameters are reported in Figure S5. We report the number average particle diameter

$$d_{NA} = \frac{\sum_i d_i}{\sum_i 1} \quad (S12)$$

while the volume-area particle diameter

$$d_{VA} = \frac{\sum_i d_i^3}{\sum_i d_i^2} \quad (S13)$$

was used to compute the Rh dispersion (D) and CO saturation coverage assuming equal exposure of the (111), (110), and (100) facets:

$$D = \frac{6 v_{Rh}}{d_{VA} a_{Rh}} \quad (S14)$$

where $v_{Rh} = 13.78 \text{ \AA}^3$ is the volume per Rh atom in the bulk metal and $a_{Rh} = 7.58 \text{ \AA}^2$ is the average exposed area per Rh atom among the three crystal facets listed above.² The number average diameter of the distribution in Figure S5 is $2.6 \pm 1.1 \text{ nm}$ (one standard deviation) and the volume-area diameter is 3.5 nm.

Section S4. CO binding to Rh₂₀₁ nanoparticles

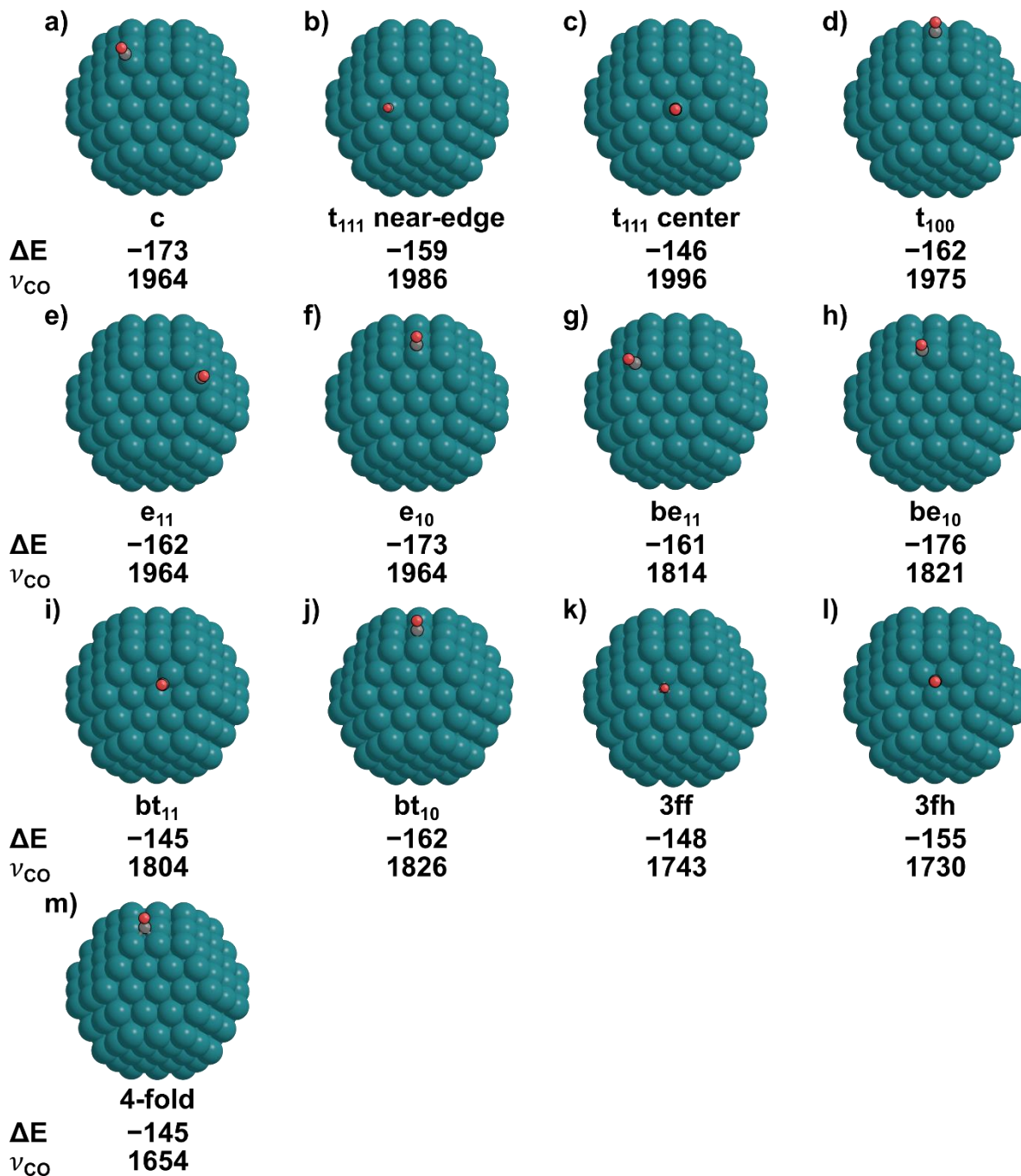


Figure S5. The binding energies (ΔE , kJ mol⁻¹) and frequencies (ν_{CO} , cm⁻¹) for CO* when bound (a) to a corner site, (b) atop the (111) terrace near the edge, (c) atop the middle of the (111) terrace, (d) atop the (100) terrace, (e) atop the edge between two (111) terraces, (f) atop the edge between (111) and (100) terraces, (g) bridge between two (111) terraces, (h) bridge between (111) and (100) terraces, (i) bridge on the (111) terrace, (j) bridge on the (100) terrace, (k) 3-fold fcc, (l) 3-fold hcp, and (m) 4-fold.

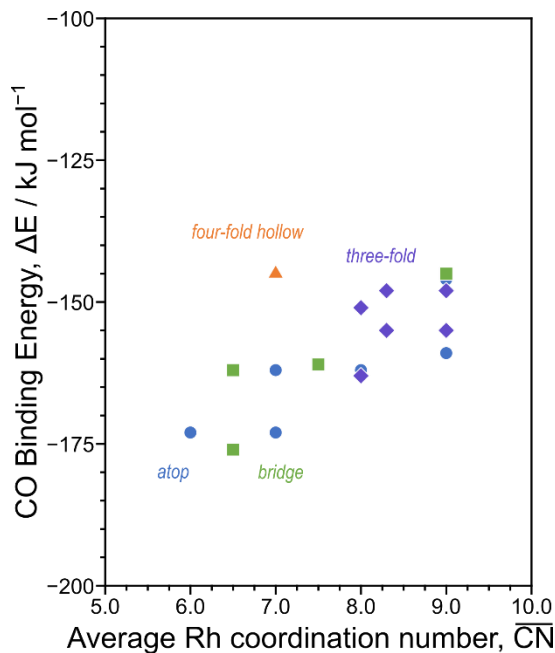


Figure S6. Binding energies of a single CO* on Rh₂₀₁ as a function of the average coordination number (CN) of the metal atoms to which CO* is bound for CO* bound atop (●, blue), bridge (■, green), three-fold (◆, purple), and four-fold (▲, orange).

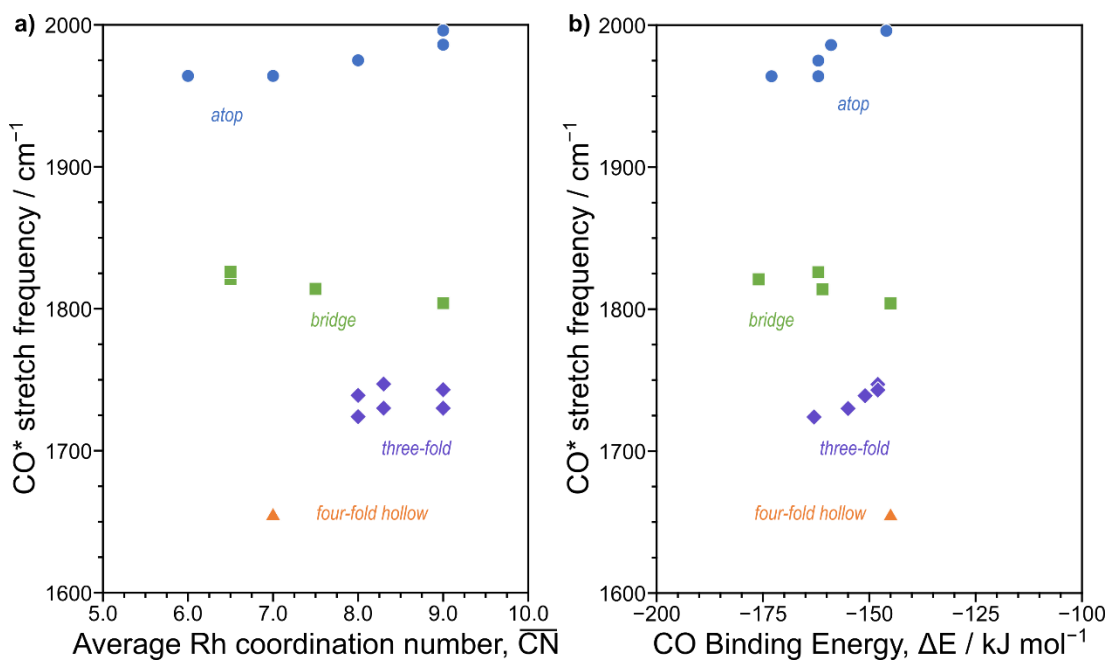


Figure S7. Stretching frequencies of a single CO* on Rh₂₀₁ as functions of (a) the average coordination number (CN) of the metal atoms to which CO* is bound and (b) the binding energy for CO* bound atop (●, blue), bridge (■, green), three-fold (◆, purple), and four-fold (▲, orange).

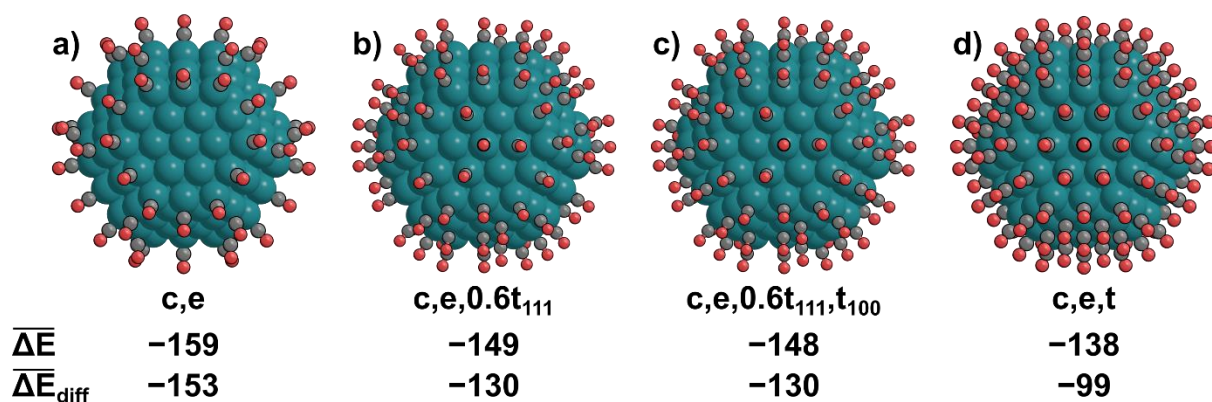


Figure S8. Configurations of CO* with their overall average ($\overline{\Delta E}$) and average differential ($\overline{\Delta E}_{diff}$) binding energies in kJ mol^{-1} for filling the Rh₂₀₁ particle with all CO* bound atop, beginning from (a) CO* bound to c and e sites and followed by (b) partial filling of the (111) terrace (c,e,0.6t₁₁₁), (c) filling the (100) terrace (c,e,0.6t₁₁₁,t₁₀₀), and (d) filling all remaining terrace sites (c,e,t).

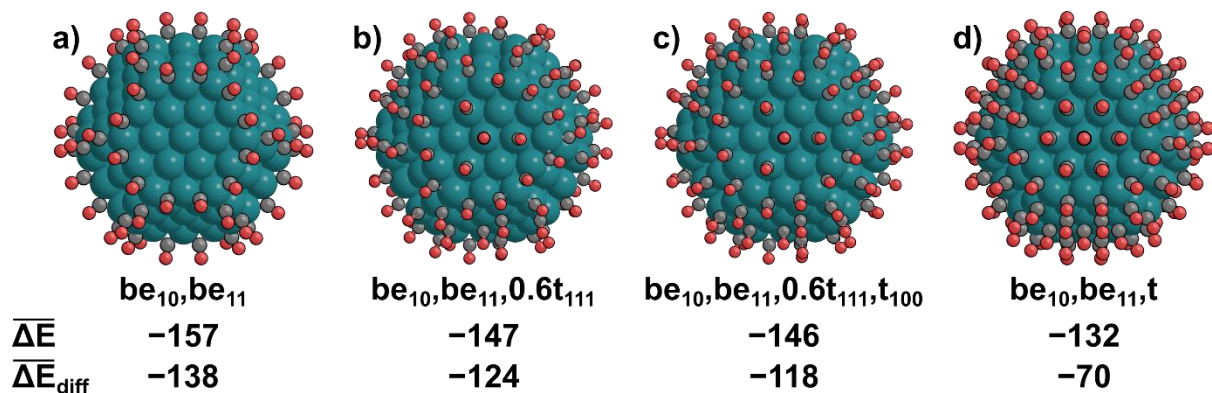


Figure S9. Configurations of CO* with their overall average ($\overline{\Delta E}$) and average differential ($\overline{\Delta E}_{diff}$) binding energies in kJ mol^{-1} for filling the Rh₂₀₁ particle with CO* filling bridge-edge and terrace sites, beginning from (a) CO* bound to be₁₀ and be₁₁ sites and followed by (b) partial filling of the (111) terrace (be₁₀,be₁₁,0.6t₁₁₁), (c) filling the (100) terrace (be₁₀,be₁₁,0.6t₁₁₁,t₁₀₀), and (d) filling all remaining terrace sites (be₁₀,be₁₁,t).

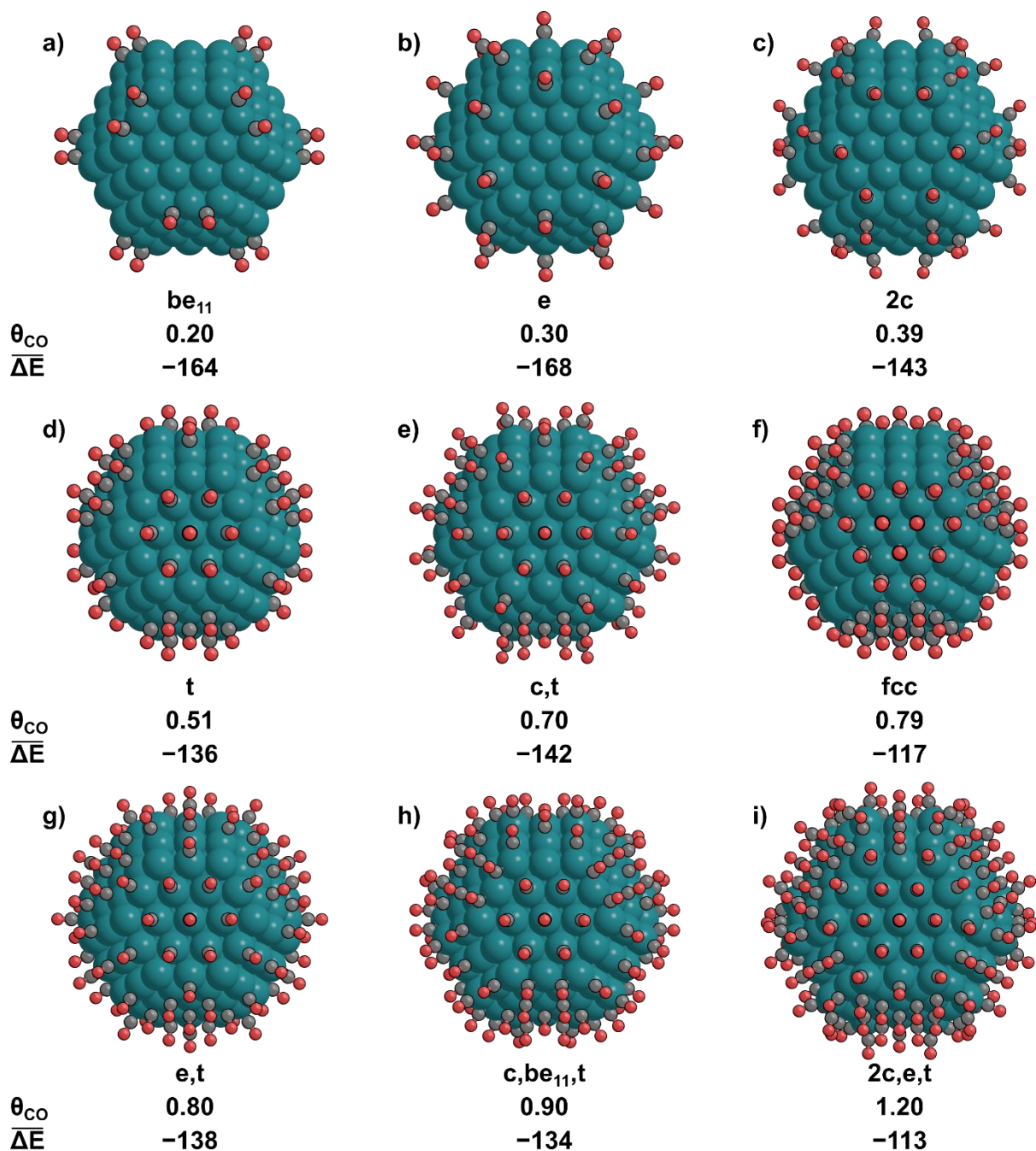


Figure S10. Other configurations of CO* on Rh₂₀₁ where the CO* adlayer did not restructure during optimization, with CO* bound to (a) be₁₁, (b) e, (c) c twice, (d) t, (e) c,t, (f) fcc, (g) e,t, (h) c,be₁₁,t, and (i) 2c,e,t sites. The CO* coverage (θ_{CO} in ML) and the average CO* binding energy ($\overline{\Delta E}$ in kJ mol⁻¹) are shown beneath each corresponding structure.

Section S5. NO binding on Rh(111)

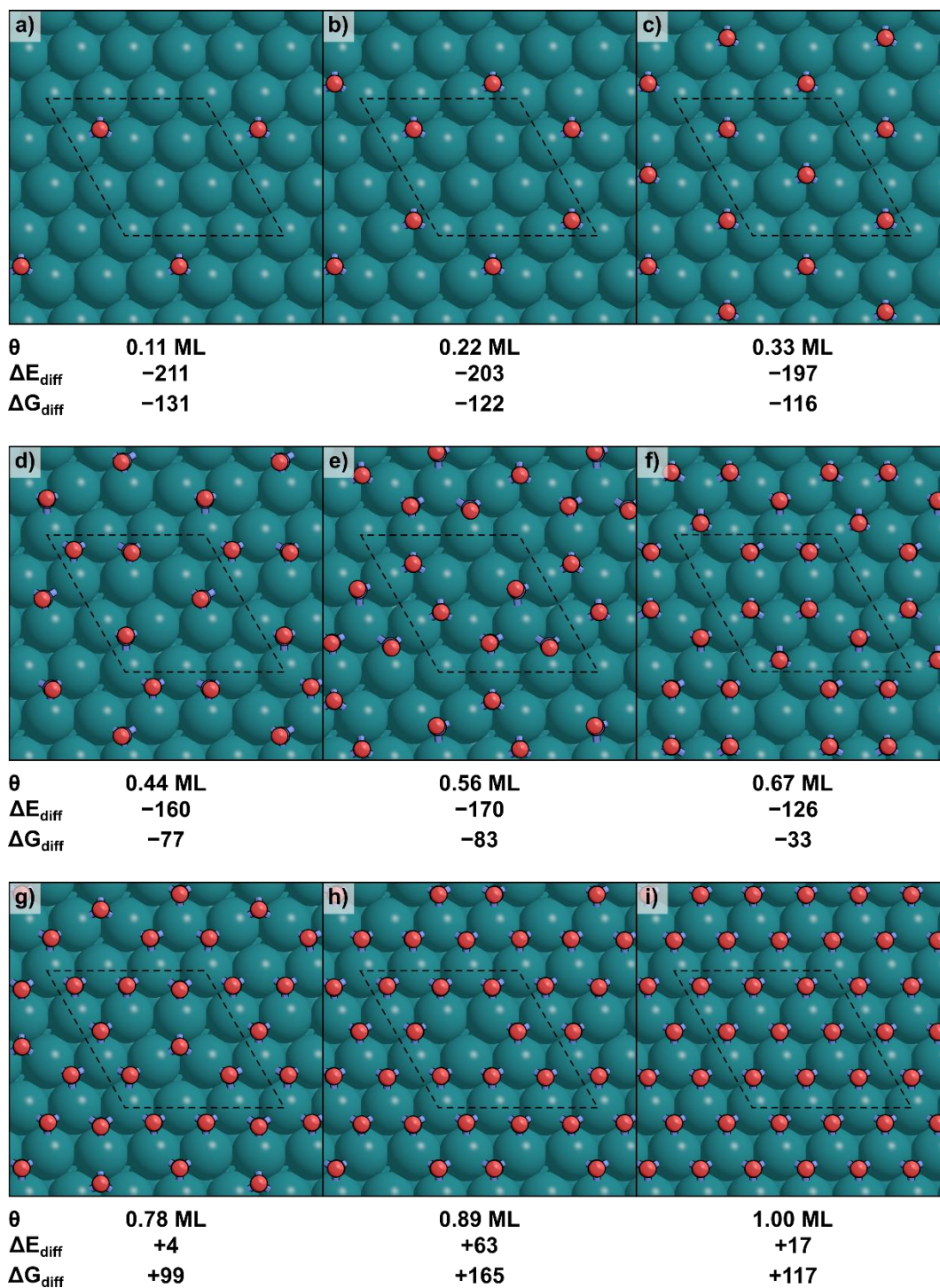


Figure S11. The lowest energy configurations of NO* on Rh(111). Differential binding electronic energies (ΔE_{diff}) and free energies (ΔG_{diff}) are shown beneath each corresponding structure in kJ mol^{-1} .

Table S4. DFT-calculated frequencies (ν_{NO} , all scaled by $\times 1.019$) and their predicted intensities for the most intense and second most intense frequencies of NO* on Rh(111) for the lowest energy configuration from 0.11–1.00 ML.

$\theta_{\text{NO}} / \text{ML}$	Binding mode	Most intense frequency		Second most intense frequency	
		$\nu_{\text{CO}} / \text{cm}^{-1}$	Intensity	$\nu_{\text{CO}} / \text{cm}^{-1}$	Intensity
0.11	3-fold hcp	1529	12.9		
0.22	3-fold hcp	1560	21.3	1534	0.1
0.33	3-fold hcp	1582	27.0	1544	0.0
0.44	3-fold mixed	1633	27.4	1554	0.8
0.56	3-fold mixed	1673	28.4	1580	0.7
0.67	3-fold mixed	1735	19.4	1653	8.1
0.78	3-fold mixed	1712	23.1	1583	0.3
0.89	3-fold fcc	1730	19.3	1615	0.1
1.00	3-fold fcc	1744	18.2	1617	0.0

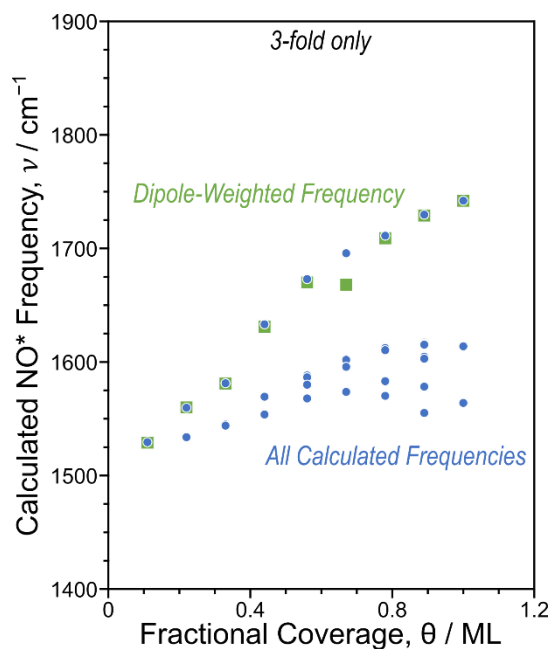


Figure S12. All calculated frequencies for NO* on Rh(111) from 0.11–1.00 ML (●, blue) with in the most favorable configuration, where all NO* remain preferably 3-fold bound. The average frequency based on weights derived from DFT-predicted intensities with the estimated dipole are shown at each coverage (■, green).

Section S6. NO* binding to Rh₂₀₁ nanoparticles

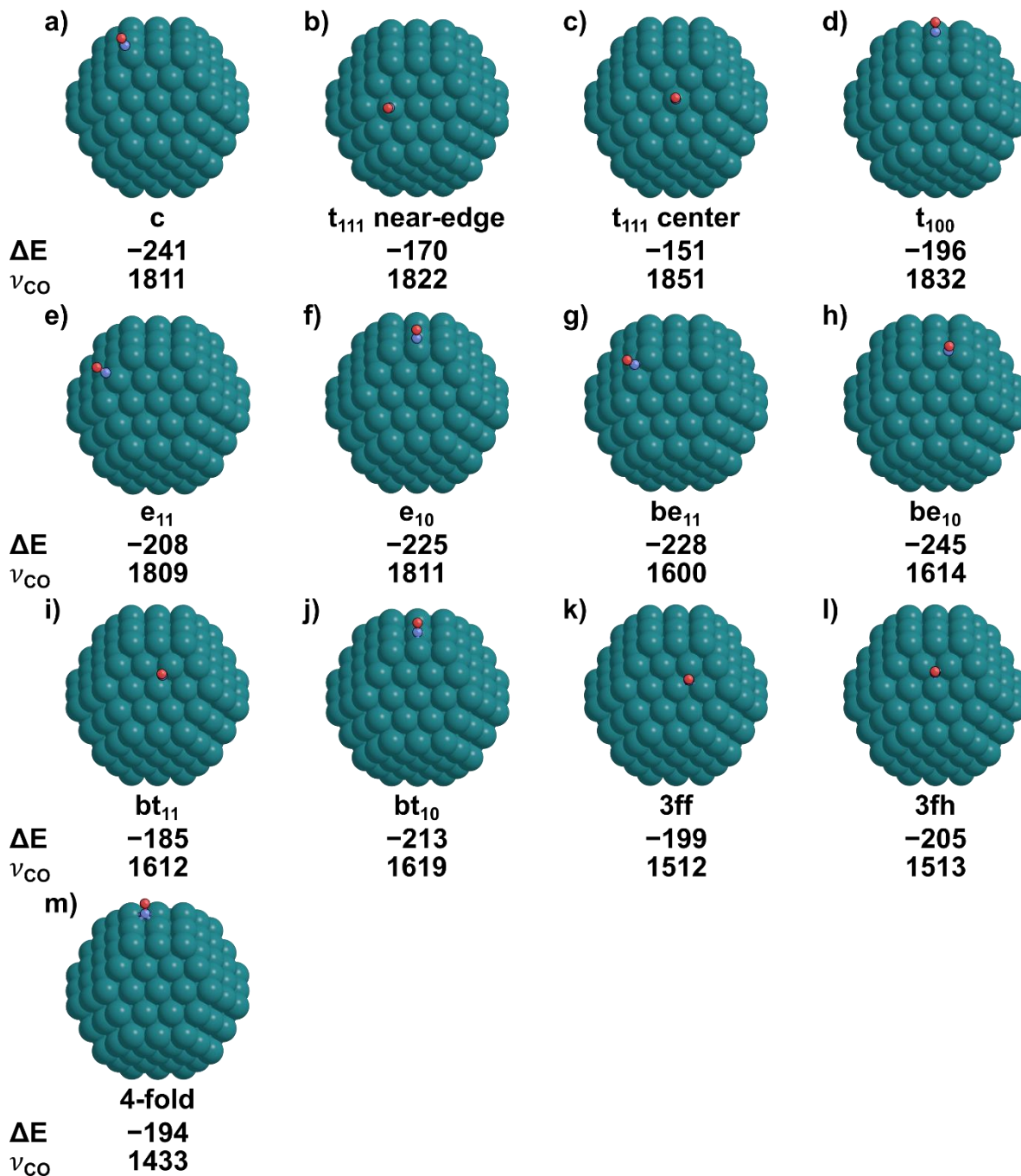


Figure S13. The binding energies (ΔE , kJ mol⁻¹) and frequencies (ν_{NO} , cm⁻¹) for NO* when bound (a) to a corner site, (b) atop the (111) terrace near the edge, (c) atop the middle of the (111) terrace, (d) atop the (100) terrace, (e) atop the edge between two (111) terraces, (f) atop the edge between (111) and (100) terraces, (g) bridge between two (111) terraces, (h) bridge between (111) and (100) terraces, (i) bridge on the (111) terrace, (j) bridge on the (100) terrace, (k) 3-fold fcc, (l) 3-fold hcp, and (m) 4-fold.

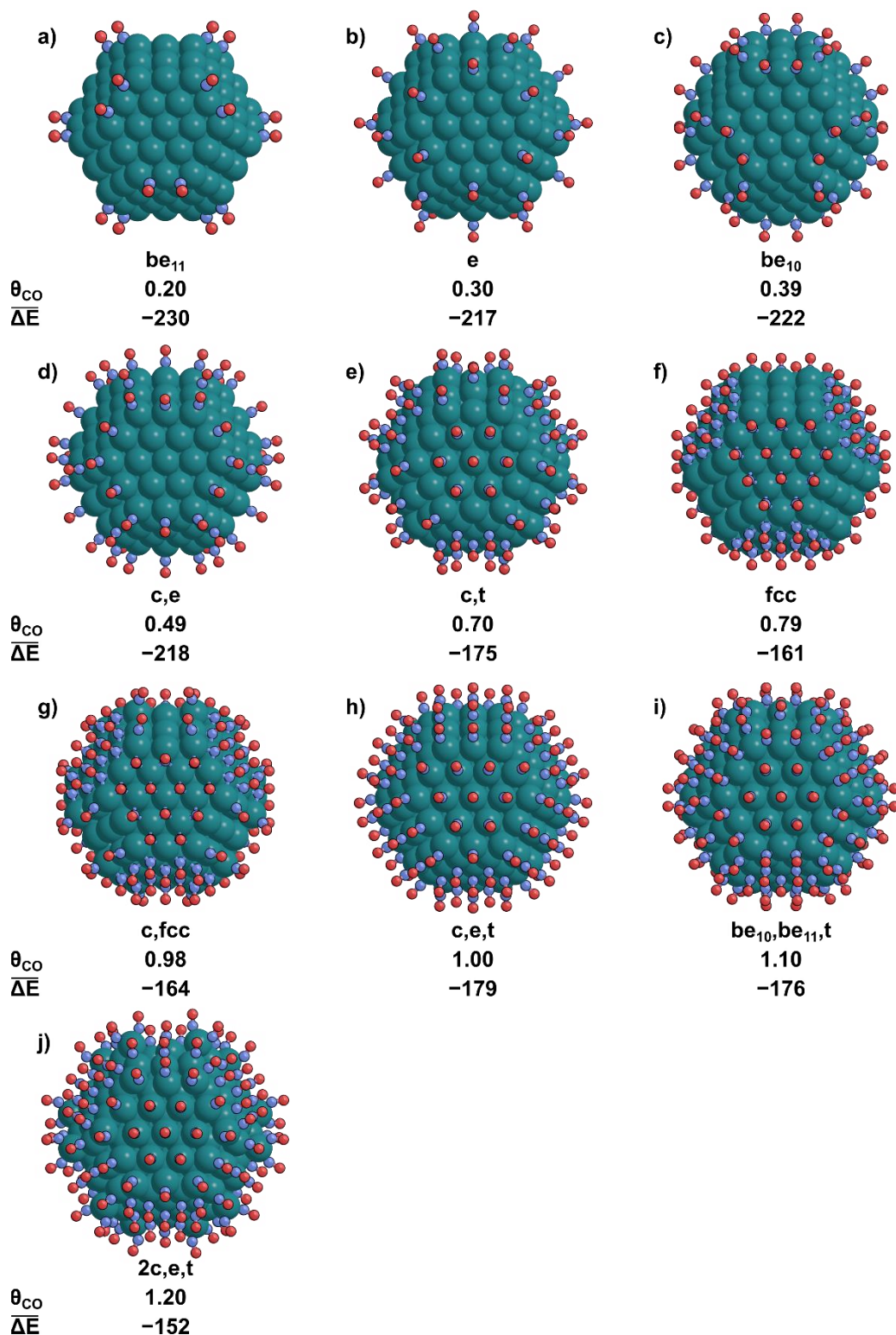


Figure S14. Other configurations of NO* on Rh₂₀₁ where the NO* adlayer did not restructure during optimization, with NO* bound to (a) be₁₁, (b) e, (c) c twice, (d) t, (e) c,t, (f) fcc, (g) e,t, (h) c,be₁₁,t, and (i) 2c,e,t sites. The CO* coverage (θ_{NO} in ML) and the average NO* binding energy ($\overline{\Delta E}$ in kJ mol⁻¹) are shown beneath each corresponding structure.

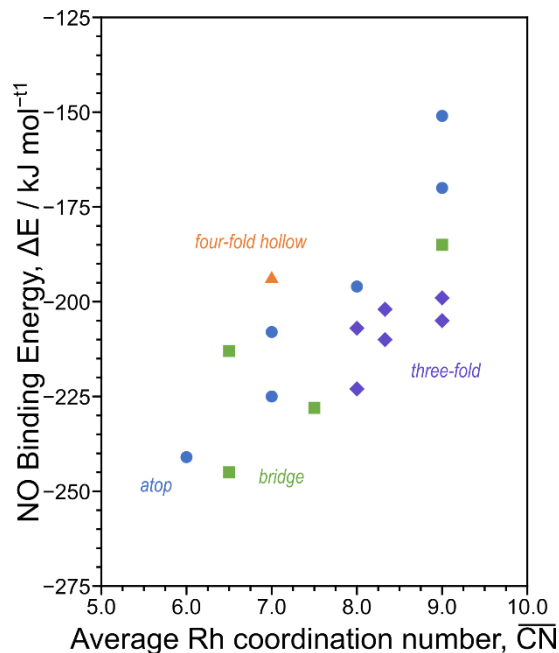


Figure S15. Binding energies of a single NO* on Rh₂₀₁ as a function of the average coordination number (CN) of the metal atoms to which NO* is bound for NO* bound atop (●, blue), bridge (■, green), three-fold (◆, purple), and four-fold (▲, orange).

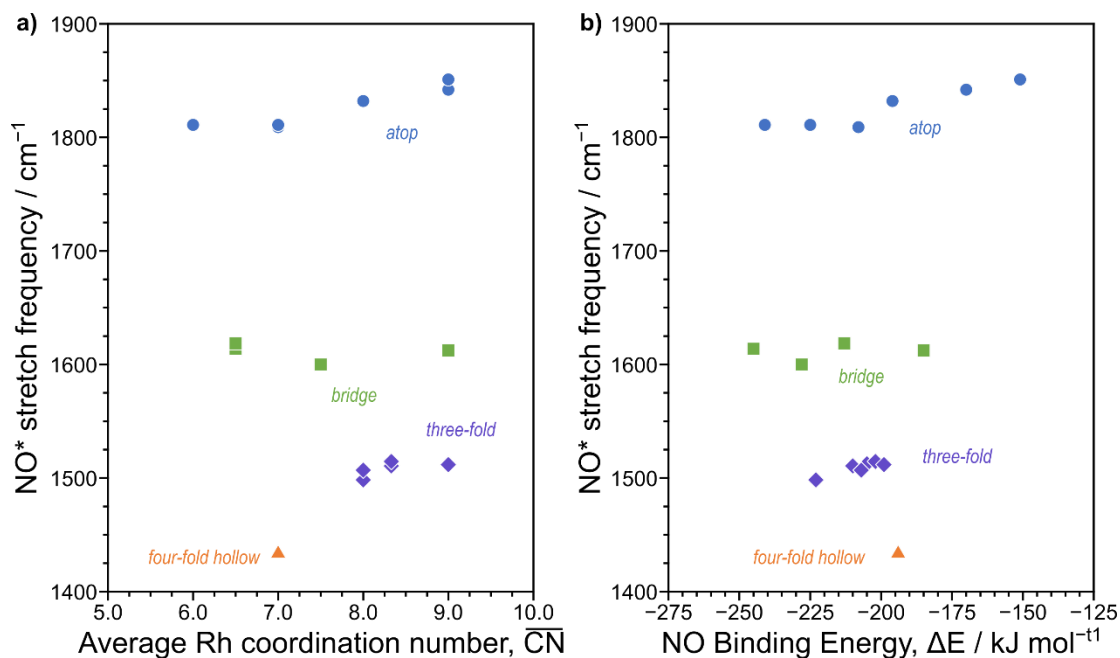


Figure S16. Stretching frequencies of a single NO* on Rh₂₀₁ as functions of (a) the average coordination number (CN) of the metal atoms to which NO* is bound and (b) the binding energy for NO* bound atop (●, blue), bridge (■, green), three-fold (◆, purple), and four-fold (▲, orange).

Section S7. NO-CO exchange and mixtures

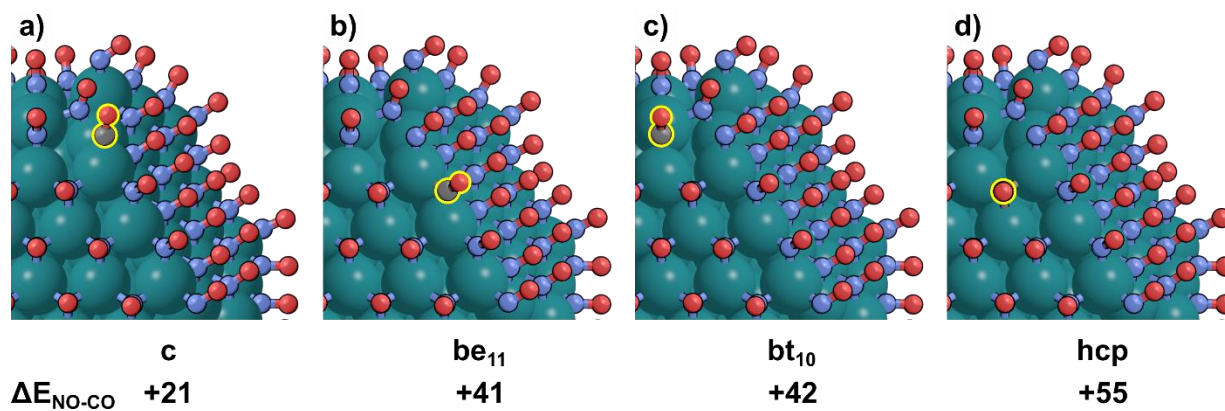


Figure S17. Rh₂₀₁ particles at 1.38 ML of NO* where one NO* is replaced by CO* in each unique binding mode: (a) on a corner site, (b) on a be₁₁ site, (c) on a bt₁₀ site, and (d) in a three-fold hcp site. The energy to exchange NO for CO ($\Delta E_{\text{NO-CO}}$) is shown beneath each structure in kJ mol⁻¹.

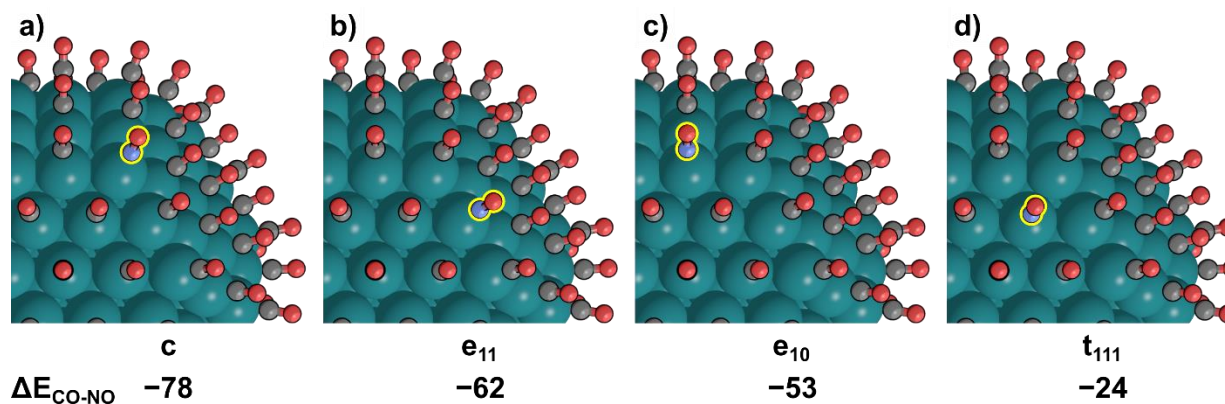


Figure S18. Rh₂₀₁ particles at 1.00 ML of CO* where one CO* is replaced by NO* in each unique binding mode: (a) on a corner site, (b) on an e₁₁ site, (c) on an e₁₀ site, and (d) on a t₁₁₁ site. The energy to exchange CO for NO ($\Delta E_{\text{CO-NO}}$) is shown beneath each structure in kJ mol⁻¹.

References

- (1) McQuarrie, D. A. *Statistical mechanics*; University Science Books: Sausalito, Calif, 2000.
- (2) Bergeret, G.; Gallezot, P. In *Handbook of heterogeneous catalysis: online*; Ertl, G.; Knözinger, H.; Schüth, F.; Weitkamp, J., Eds.; Wiley-VCH Verlag GmbH & Co. KGaA: Weinheim, Germany, 2008.